Atmospheric Research 237 (2020) 104810

Contents lists available at ScienceDirect

Atmospheric Research

journal homepage: www.elsevier.com/locate/atmosres

A 17-year climatology of temperature inversions above clouds over the ARM SGP site: The roles of cloud radiative effects

Jinqiang Zhang[a,b,c], Youtong Zheng[d], Zhanqing Li[d,*], Xiangao Xia[a,b,c], Hongbin Chen[a,b,c]

[a] Key Laboratory of Middle Atmosphere and Global Environment Observation, Institute of Atmospheric Physics, Chinese Academy of Sciences, Beijing 100029, China
[b] Collaborative Innovation Center on Forecast and Evaluation of Meteorological Disasters, Nanjing University of Information Science & Technology, Nanjing 210044, China
[c] University of Chinese Academy of Sciences, Beijing 100049, China
[d] Earth System Science Interdisciplinary Center, University of Maryland, College Park, MD 20740, USA

ARTICLE INFO

Keywords:
Atmospheric temperature inversion
Cloud
Radiative cooling
Radiosonde dataset

ABSTRACT

Atmospheric temperature inversions, i.e., temperatures increasing with altitude, modulate both radiative and buoyancy fluxes in the atmosphere. A temperature inversion layer often occurs immediately above a cloud layer that cools radiatively and thereby strengthens the capping temperature inversion. This study aims to investigate the characteristics of temperature inversions above clouds and their relationships with cloud-top radiative cooling. Using a 17-year (January 2001 to December 2017) high-quality and continuous radiosonde dataset collected at the Atmospheric Radiation Measurement Southern Great Plains Central Facility site, key temperature inversion parameters, namely, the occurrence frequency (dp), depth (dz), temperature difference (dT), and gradient (dT/dz), are derived for single- and double-layer clouds (SLC and DLC, respectively). The occurrence frequency of temperature inversions above single-layer clouds decreases dramatically as cloud tops rise from low to high altitudes. When an overlying higher cloud layer is present, the inversion becomes less frequent, shallower, and weaker than without it. This may be because higher clouds weaken the cloud-top radiative cooling of the underneath clouds by enhancing downwelling infrared radiation. This is supported by radiative transfer simulations. There are distinctive seasonal cycles of cloud-top radiative cooling for high clouds that are primarily driven by variations in shortwave heating. Distinctive seasonal cycles of temperature inversions also occurred regardless of the cloud regime (SLC or DLC) and altitude (low or high clouds). They appear to be driven by the seasonal cycle of cloud coverage (i.e., a greater amount of clouds undergoes stronger area-mean radiative cooling) although the shortwave heating seasonal cycle also plays a role for high clouds. Cloud radiative cooling cannot explain the diurnal cycle of temperature inversions.

1. Introduction

Clouds affect the radiation budget of the earth's atmosphere by reflecting the incoming solar radiation, absorbing the upwelling infrared radiation, and then re-emitting it at generally lower temperatures (Stephens et al., 2012). The radiative heating/cooling caused by clouds couple strongly with atmospheric dynamics, thermodynamics, and the hydrological cycle (Del Genio et al., 2005; Kalesse and Kollias, 2013). Despite the critical importance of clouds in the formation of the earth's climate, clouds and their climatic effects remain the largest uncertainties in modeling climate and its changes.

As a common atmospheric feature, the atmospheric temperature inversion, i.e., an inversion of the thermal lapse rate, impacts both radiative and turbulent heat fluxes and partly determines local climate feedbacks (Pithan et al., 2013). There are complicated mutual interactions between clouds and their overlying temperature inversions. On the one hand, an inversion helps trap moisture within the underlying layers and thus favors cloud formation (Klein and Hartmann, 1993; Wood and Bretherton, 2006; Solomon et al., 2011). This effect has been extensively studied and applied in many cloud-related studies. For example, the lower-tropospheric stability (LTS, defined as the potential temperature difference between the surface and 700 hPa) as a proxy for cloud-top temperature inversions has been widely used to parameterize cloud coverage and to classify cloud regimes. On the other hand, clouds enhance the temperature inversion through radiative and evaporative cooling (Wood, 2012; Zheng et al., 2016). This effect, however, has been less studied. This study focuses on the cloud-top radiative cooling effects on temperature inversions. A practical reason for not considering evaporative cooling is the extreme difficulty of quantifying it in observations and numerical models (Lolli

* Corresponding author.
E-mail address: zli@atmos.umd.edu (Z. Li).

https://doi.org/10.1016/j.atmosres.2019.104810
Received 21 July 2019; Received in revised form 7 November 2019; Accepted 19 December 2019
Available online 24 December 2019

et al., 2017). Note that these two cooling mechanisms are principally correlated with each other because the radiative-cooling-driven turbulent mixing can enhance the cloud-top entrainment rate, thereby increasing the evaporative cooling (Bretherton and Wyant, 1997). The radiative cooling can be obtained from a radiative transfer model that ingests radiosonde-observed temperature and moisture profiles and cloud boundaries (Ghate et al., 2014; Wood, 2005; Zheng et al., 2016, 2018, 2019).

Radiosonde measurements, which can provide detailed profiles of temperature, pressure, dew point, and horizontal winds, are ideal for studying temperature inversions (Seidel et al., 2010). Radiosonde data have been widely used to characterize the temporal variations of inversions (e.g., Bradley et al., 1992; Miller et al., 2013; Serreze et al., 1992). More importantly, radiosondes can also penetrate cloud layers and thus likely can provide significant information about clouds, for example, the locations and boundaries of cloud layers (e.g., Chernykh and Eskridge, 1996; Minnis et al., 2005; Naud et al., 2003; Wang et al., 2000). Wang and Rossow (1995) used relative humidity (RH) profiles to derive the cloud vertical structure. Applying a modified version of the method described by Wang and Rossow (1995), radiosonde data obtained from the US Department Energy's Atmospheric Radiation Measurement (ARM) mobile facility campaign at Shouxian, China in 2008 were used to derive the vertical distributions of clouds (Zhang et al., 2010).

While atmospheric temperature inversions have been studied extensively (e.g., Bourne et al., 2010; Li et al., 2015; Fochesatto, 2015), to our knowledge, a quantitative assessment of temperature inversions above clouds has not yet been performed over a long period. As such, this study attempts to characterize the temporal variations of above-cloud temperature inversions. The climatological features of temperature inversions and clouds are valuable for both understanding and modeling clouds. The synergetic long-term observations made under the aegis of the ARM program can facilitate this effort. In this study, seventeen years (January 2001 to December 2017) of radiosonde data collected at the Southern Great Plains Central Facility (SGP) site are used to derive cloud boundaries and temperature inversions above cloud tops. While ground-based cloud radar has provided the high quality, good continuity and long duration of cloud measurements at the SGP site, given the following factors, we think that additional observations are desperately needed to improve our understanding of the cloud properties. The radiosonde-based atmospheric profile data can convey valuable and independent/complementary information to the radar observations. Moreover, radiosonde data from around the world have been collected routinely for many decades, whereas only a handful of ARM-like stations have been established over the past decade. Detailed observations of cloud properties can't be available globally provided that we are limited to the ground-based instruments such as those developed by the ARM project. Therefore, we use the long-term radiosonde measurements to investigate the climatological features of the occurrences, depths, differences, and gradients of temperature inversions over the tops of clouds. Since clouds in different vertical layers dictate the adiabatic heating rate and the radiation balance of the atmospheric column, a quantitative assessment is also conducted for two different cloud categories (i.e., low and high clouds).

The paper is organized as follows. Section 2 introduces the data and detection algorithms of cloud layers and temperature inversions. Section 3 presents the climatological characteristics of temperature inversions above cloud and their temporal variations. Section 4 summarizes the main conclusions.

2. Data and methodology

2.1. Data

A large number of remote sensing instruments have been deployed at the ARM SGP site [(36.61°N, 97.49°W); 315 m above sea level] in north-central Oklahoma since 1992. Routine radiosonde launches have been maintained over two decades, chiefly four times a day at 0530, 1130, 1730, and 2330 UTC, with up to eight launches during intensive field experiments such as the Atmospheric Infrared Sounder Campaign (Tobin et al., 2006). Radiosonde type used at the SGP site was mostly Vaisala RS9x model during the periods we concerned; the new Vaisala RS41 model was used from fall of 2013 onward. It was indicated that the differences between their measurements should have little impact for many science applications (Jensen et al., 2016). A radiosonde measures pressure, temperature, RH, wind speed, and wind direction every 2 s at an average ascent rate of about 5 m s^{-1}, resulting in a high vertical resolution of ~10 m. Radiosonde data from the SGP site (datastream of sgpsondewnpnC1.a1) are of high quality and good continuity over the period 2001–2017. A total of 23,668 profiles were collected for this study. Only radiosonde data reaching altitudes exceeding 10 km are used, which account for 97.2% of all profiles.

2.2. Cloud detection using radiosonde data

The radiosonde-based cloud retrieval algorithm of Zhang et al. (2010), which was significantly modified from Wang and Rossow (1995), was used to detect cloud boundaries. Zhang et al. (2013) further carried out an extensive validation of radiosonde-based cloud detection against a ground-based remote sensing product at multiple ARM sites (including the SGP site) located in different climate regimes, which showed a good agreement. It should also be noted that it is challenging to perform the strict evaluation given their respective advantages/limitations inherent in the two different cloud retrieval methods (i.e., remote sensing and in-situ measurements), the object mismatch caused by a fixed ground-based instrument and a drifting balloon, and the different temporal resolutions of the two datasets (Zhang et al., 2014).

A description of the radiosonde-based cloud retrieval algorithm is presented here for completeness while details can be found in Zhang et al. (2010, 2013). The algorithm employs three height-resolving RH thresholds to determine cloud layers, i.e., minimum and maximum RH thresholds (min-RH and max-RH) in cloud layers, as well as the minimum RH threshold within the distance between two neighboring cloud layers (inter-RH). The RH is transformed with respect to ice for levels with temperatures below 0 °C. Cloud layers are then identified according to the main following steps: 1) the base of the lowest moist layer is determined as the level where RH exceeds the min-RH corresponding to this level; 2) levels above the base of the moist layer with RH greater than the min-RH are treated as the same layer; 3) the top of the moist layer is identified where RH decreases to the min-RH; 4) the moist layer is classified as a cloud layer if the maximum RH within this layer is higher than the corresponding max-RH at the base of this moist layer; 5) the base of cloud layers is set to 136 m above ground level; 6) two neighboring cloud layers are considered as a one-layer cloud if the distance between these two layers is < 300 m or the minimum RH within this distance is greater than the maximum inter-RH value within this distance; and 7) clouds are discarded if their thicknesses are < 30.5 m for low clouds and 61 m for middle/high clouds.

Only radiosonde retrieved single- and double-layer clouds (SLC and DLC, respectively) are investigated, i.e., the radiosonde profiles with more than two-layer clouds determined are excluded by this study. The SLC and DLC dominate the radiosonde-based cloud populations (77.4%) at the SGP site.

2.3. Above-cloud temperature inversion identification

The approach of Zhang et al. (2016) is employed to determine the temperature inversion above a cloud and is specified as follows. The method uses the first-order derivative of the temperature profile with respect to height to determine the temperature inversion layer. The temperature difference across each thin layer is calculated by scanning upwards from the surface to the top of the profile to find cases with

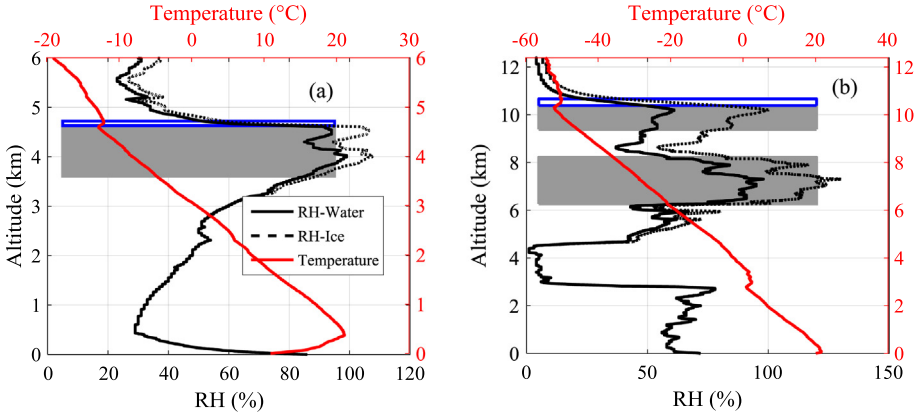

Fig. 1. Temperature inversions above (a) an SLC at 11:30 UTC 26 April 2001 and above (b) DLC at 23:29 UTC 6 November 2001. Gray shading marks the extent of the cloud layer. The blue rectangles outline the temperature inversion layer. Radiosonde vertical profiles of relative humidity (RH) with respect to water, RH with respect to ice when temperatures are < 0 °C, and ambient temperature are shown by the solid black lines, the dashed black lines, and the solid red lines, respectively. (For interpretation of the references to colour in this figure legend, the reader is referred to the web version of this article.)

temperature increasing with altitude. The temperature inversion layer is defined as those contiguous levels with first-order derivatives greater than zero. Within a thick temperature inversion, thin layers that are not temperature inversions may occasionally be present. If these layers are very thin (i.e., < 50 m), they are considered to be embedded within the overall temperature inversion. The depth of the temperature inversion layer needs to exceed 15 m to be larger than the vertical resolution of radiosonde data. Only those temperature inversions with base heights < 200 m away from cloud-top heights are considered here to ensure that above-cloud temperature inversions are highly related to cloud processes. There are likely multilayered temperature inversions above the cloud top, so only the first temperature inversion layer above the cloud top is considered.

Four parameters associated with temperature inversions are defined: (1) The occurrence frequency (dp in units of %) which is defined as the number of cloud layers with temperature inversions above the cloud tops divided by the total number of cloud layers, (2) the depth of the temperature inversion (dz in units of m) which is the height difference between the top height and base height of the temperature inversion layer, (3) the temperature difference across the temperature inversion (dT in units of °C) which is defined as the temperature difference at the top height and base height of the temperature inversion layer, and (4) the temperature gradient across the temperature inversion [dT/dz in units of °C (0.1 km)$^{-1}$] which is defined as dT divided by dz. The temperature gradient, of the four parameters, has the weakest signal so is not discussed in any great detail in this paper.

3. Observational results and physical interpretations

3.1. Physical principles

To assist with the interpretation of the observational results, we briefly describe how cloud-top radiative cooling depends on cloud properties and meteorological conditions by assuming a gray-body-atmosphere theoretical framework. The cloud-top radiative cooling rate ($CTRC_{NET}$) has two components: LW cooling ($CTRC_{LW}$) and SW warming ($CTRW_{SW}$). In a gray body atmosphere, the $CTRC_{LW}$ for a single-layer cloud is quantified as.

$$CTRC_{LW} = f_{c1}(\varepsilon_{c1}\sigma T_{c1}^4 - \varepsilon_{a2}\sigma T_{a2}^4) + (1 - f_{c1})(\varepsilon_{a1}\sigma T_{a1}^4 - \varepsilon_{a2}\sigma T_{a2}^4), \quad (1)$$

where f, ε, σ, and T are the cloud fraction, the emissivity, the Stefan-Boltzmann constant (5.670367×10^{-8} kg s^{-3} K^{-4}), and effective temperature, respectively. The subscripts c1, a1, and a2 stand for the cloud, the atmosphere below the altitude of the cloud top in cloud-free regions, and the atmosphere overlying the clouds. The clear-sky component $\varepsilon_{a1}\sigma T_{a1}^4 - \varepsilon_{a2}\sigma T_{a2}^4$ (several K day^{-1}) is typically a magnitude smaller than the cloudy component $\varepsilon_{c1}\sigma T_{c1}^4 - \varepsilon_{a2}\sigma T_{a2}^4$, so the equation can be simplified to.

$$CTRC_{LW} = f_{c1}(\varepsilon_{c1}\sigma T_{c1}^4 - \varepsilon_{a2}\sigma T_{a2}^4) = f_{c1}CTRC^*_{LW}. \quad (2)$$

This equation highlights several key influential factors of LW radiative cooling that should be considered. First, the $CTRC_{LW}$ is linearly proportional to the cloud fraction and cloud emissivity that is a function of cloud optical depth (Stephens et al., 1990). A more extensive cloud layer with a greater optical depth tends to cool the overlying air layer more, thereby leading to a stronger temperature inversion. Here, we use $CTRC^*_{LW}$ to denote the LW radiative cooling under fully cloudy conditions. Second, $CTRC_{LW}$ is proportional to the fourth power of the cloud-top temperature. Third, $CTRC_{LW}$ is compensated by downwelling radiation that is governed by the water vapor burden of the overlying atmosphere (Mapes and Zuidema, 1996; Zheng et al., 2016). If there is an overlying cloud layer, an additional cloud emission term should be added: $-\varepsilon_{c2}\sigma T_{c2}^4$. This suggests that the occurrence of an overlying cloud layer can weaken the LW cooling of the underlying clouds. As will be shown later, such weakening effects on $CTRC_{LW}$ can considerably reduce the occurrence frequency of the temperature inversion for the lower cloud.

The $CTRW_{SW}$ always compensates for the $CTRC_{LW}$ by absorbing solar radiation, and the degree of the compensation largely depends on the solar zenith angle and water vapor amount above clouds. Since a considerable fraction of the absorption bands by water vapor and cloud droplets are overlapped, absorption by clouds and the water column depends critically on their vertical distributions (Li and Moreau, 1996). Under most conditions, however, the $CTRW_{SW}$ is less than the $CTRC_{LW}$, leaving a net radiative cooling at cloud tops (Wood, 2012).

3.2. Case study and probability of all temperature inversions

Fig. 1 shows how the temperature inversion structure is determined above an SLC at 11:30 UTC 26 April 2001 and above DLC at 23:29 UTC 6 November 2001. Gray shading shows the extents of the cloud layers retrieved from radiosonde measurements. A temperature inversion layer was identified above the SLC (Fig. 1a). Its dz, dT, and dT/dz were 91 m, 0.50 °C, and 0.55 °C (0.1 km)$^{-1}$, respectively. For the DLC (Fig. 1b), one temperature inversion layer with dz, dT, and dT/dz values of 279 m, 1.4 °C, and 0.5 °C (0.1 km)$^{-1}$ was retrieved above the higher cloud. No temperature inversion layer was detected above the lower cloud.

Fig. 2 shows histograms of the temperature inversion parameters for all SLCs, the lower cloud in the DLC configuration, and the higher cloud in the DLC configuration. All histograms are highly skewed to smaller values. The occurrence frequency of dz reaches a maximum at 40 m then gradually deceases. The accumulated frequencies for dz < 200 m are 69.9%, 79.2%, and 68.5% for the three cloud configurations, respectively (Fig. 2a). The greatest frequency is 18–21% for dT at 0.2 °C then a slight reduction appears (Fig. 2b). The peak dT/dz occurs at 0.4 °C (0.1 km)$^{-1}$ (Fig. 2c). Most values are < 2 °C (0.1 km)$^{-1}$, which

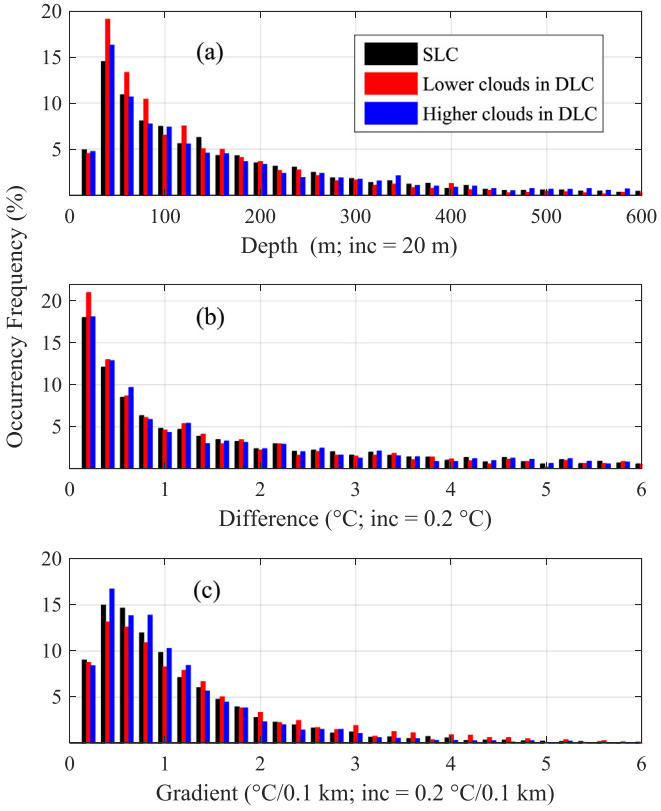

Fig. 2. Distributions of temperature inversions in terms of (a) depth (20-m bins), (b) temperature difference (0.2-°C bins), and (c) gradient [0.2 °C (0.1 km)$^{-1}$ bins] above an SLC (black bars), the lower cloud in a DLC configuration (red bars), and the higher cloud in a DLC configuration (blue bars). (For interpretation of the references to colour in this figure legend, the reader is referred to the web version of this article.)

accounts for 85.1%, 80.5%, and 87.9% of all values for the three cloud configurations, respectively.

3.3. Vertical structure

Fig. 3 shows the vertical profiles of the occurrence frequencies of cloud-top heights for SLC and DLC. While the frequencies of cloud occurrence at the time of radiosonde launch are likely different from that all day long obtained by the ground measurements due to the diurnal cycle of the cloud occurrence (Dong et al., 2006), the radiosonde-based SLC retrievals are consistent with cloud radar observations made over this region (Dong et al., 2006; Xi et al., 2010; Kennedy et al., 2014; Zhang et al., 2017), as shown by a bimodal distribution with a lower peak located in the boundary layer and an upper peak located in the high troposphere in Fig. 3. Also note that different temporal and vertical resolutions among various cloud datasets may affect the magnitude of their retrieved cloud occurrence frequency (Xi et al., 2010; Zhang et al., 2014; Kennedy et al., 2014). Ground-based radar cloud product generally has a temporal resolution of 10 s and a vertical resolution of 45 m, whereas the radiosondes are generally launched every 6 h with a vertical resolution of ~10 m. The altitudes of the two peaks in the SLC case (2 km and 12 km) match the altitudes of the peaks of the lower and higher clouds in the DLC case (Fig. 3). Such a correspondence motivates us to split the SLC samples into low (cloud top < 6 km) and high clouds (cloud top > 6 km) to match the lower and higher clouds in the DLC configuration, respectively.

Table 1 shows the statistics of temperature inversions for the four cloud types, i.e., SLC low clouds, SLC high clouds, DLC lower clouds, and DLC higher clouds. For SLC, the occurrence frequency decreases

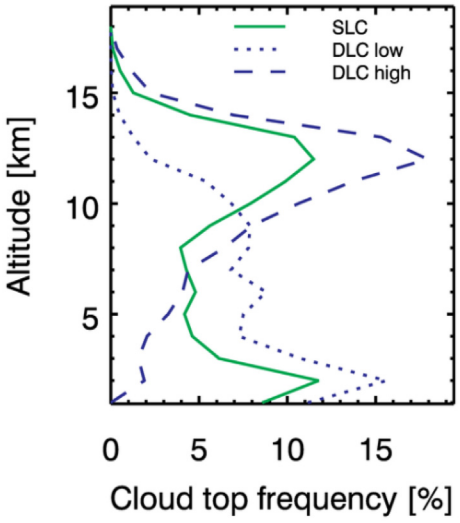

Fig. 3. Profiles of the occurrence frequencies of cloud-top heights for an SLC (solid green line), the lower cloud in a DLC configuration (short dashed blue line), and the higher cloud in a DLC configuration (long dashed blue line). (For interpretation of the references to colour in this figure legend, the reader is referred to the web version of this article.)

Table 1
Occurrence frequencies (dp in %) of temperature inversions above cloud tops for SLC low clouds, SLC high clouds, DLC lower clouds, and DLC higher clouds; and averages and standard deviations of the temperature inversion depth (dz in units of m), the temperature inversion difference (dT in units of °C), and the temperature inversion gradient [dT/dz in units of °C (0.1 km)$^{-1}$] of the four kinds of cloud configuration.

		dp (%)	dz (m)	dT (°C)	dT/dz [°C (0.1 km)$^{-1}$]
SLC	Low clouds	85.5%	189.1 ± 169.8	2.6 ± 2.6	1.7 ± 1.8
	High clouds	46.5%	219.3 ± 276.1	1.6 ± 2.0	0.8 ± 0.7
DLC	Lower clouds	40.3%	133.6 ± 135.2	1.7 ± 2.2	1.3 ± 1.4
	Higher clouds	48.4%	213.5 ± 276.3	1.8 ± 2.2	1.1 ± 1.1

dramatically from 85.5% to 46.5% as the cloud top rises from low to high altitudes. In the DLC configuration, the higher clouds have larger dp, dz, and dT relative to the lower clouds.

There are two noteworthy features in Table 1:

(1) In SLC, the temperature inversion is more frequent (larger dp), shallower (smaller dz), and stronger (larger dT) for low clouds than for high clouds.
(2) The temperature inversion is significantly stronger in terms of dp, dz, and dT for SLC low clouds than for DLC lower clouds whereas there is no marked difference between the SLC high clouds and the DLC higher clouds.

We next examine the roles of both cloud LW cooling and SW warming by running a radiative transfer model. We use the Santa Barbara DISORT Atmospheric Radiative Transfer (SBDART) model (Ricchiazzi et al., 1998). The vertical resolution is 300 m. The solar zenith angle is set to the value of the equinox noon time. The thermodynamic profiles inputted to the model are from the climatological means of the radiosonde measurements. Fig. 4a shows that there is no systematic difference in temperature profile between SLC and DLC. The atmosphere is slightly moister when DLC are present than when SLC are present (Fig. 4b). The liquid water path (LWP) and ice water path (IWP) for the low and high clouds are set as 97 and 163 g cm^{-2}, respectively.

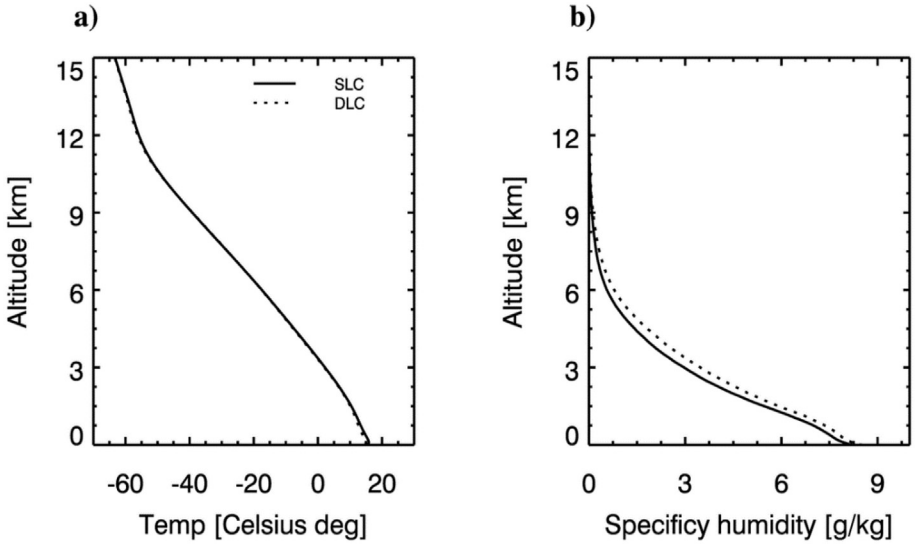

Fig. 4. Mean profiles of (a) temperature and (b) specific humidity for SLC (solid lines) and DLC (dashed lines).

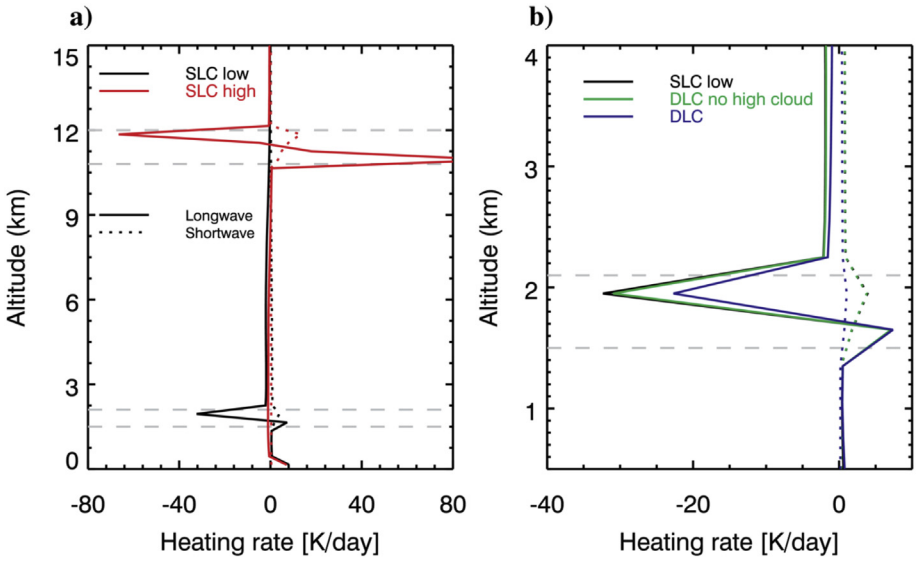

Fig. 5. Simulated atmospheric heating rates for (a) SLC low clouds (in black) and SLC high clouds (in red), and (b) DLC lower cloud with (in blue) and without (in green) a higher cloud. SLC low clouds are also shown in this panel (in black). Solid and dashed lines denote the longwave and shortwave, respectively. The horizontal dashed lines delineate cloud layers. (For interpretation of the references to colour in this figure legend, the reader is referred to the web version of this article.)

Table 2
Model-calculated $CTRC^{*}_{LW}$, $CTRW^{*}_{SW}$, and $CTRC^{*}_{NET}$ (in units of K day^{-1}) for the four simulations, i.e., SLC low cloud (SCL-low), SLC high cloud (SLC-high), DLC lower cloud (DLC-lower), and DLC lower cloud without a higher cloud (DLC-lower') in Fig. 5.

	SLC-low	SLC-high	DLC-lower	DLC-lower'
$CTRC^{*}_{LW}$	−32.43	−66.93	−22.69	−31.04
$CTRW^{*}_{SW}$	3.84	15.83	0.86	3.73
$CTRC^{*}_{NET}$	−28.59	−51.34	−21.84	−27.31

These values are their respective annual means from geostationary satellite observations over the SGP region (Wu et al., 2008). The inputted LWP and IWP are uniformly distributed over the altitude range of the cloud layer. The effective radius of the low and high clouds is set as 15 and 30 μm, respectively. Note that the main conclusions are not sensitive to the values of the effective radius. The calculated SW fluxes are divided by π to account for the diurnal cycle of the solar zenith angle (Mapes and Zuidema, 1996). Because the cloud layers specified in the model are assumed to horizontally fill the atmospheric column, i.e., cloud fraction = 1, the cloud-top LW cooling and SW heating computed by the simulations are essentially $CTRC^{*}_{LW}$ and $CTRW^{*}_{SW}$, respectively. We quantify the $CTRC^{*}_{LW}$ and $CTRW^{*}_{SW}$ by finding the minimum LW cooling and maximum SW heating rate within the cloud layers.

Note that the radiative calculation is done in a composite sense, which is somewhat rudimentary. But since we use it as a guidance for interpreting the observations (similar to that in Hartmann and Berry, 2017), not for reproducing the radiative effects, the calculation fits our purpose well. Zheng et al. (2019) show that the CTRC* is most sensitive to the above-cloud moisture loading, cloud-top temperature, and LWP. The previous two variables are well constrained by radiosonde data. The only source of uncertainty stems from the LWP. The dependence of CTRC* on the LWP is nonlinear: the dependence is strong at low LWP, but saturates when LWP $>$ 50 g m^{-2} (Kazil et al., 2016). This suggests that the composite-based calculation may have large uncertainties only for very thin clouds.

Fig. 5a shows that $CTRC^{*}_{NET}$ is stronger for high SLC than for low SLC, which seems inconsistent with our observations of temperature inversions being weaker and less frequent in high clouds. Indeed, compared with low clouds, there is less water vapor above high clouds. This weakens the downwelling infrared fluxes, thus enhancing LW cooling (Table 2). Although less above-cloud water vapor will

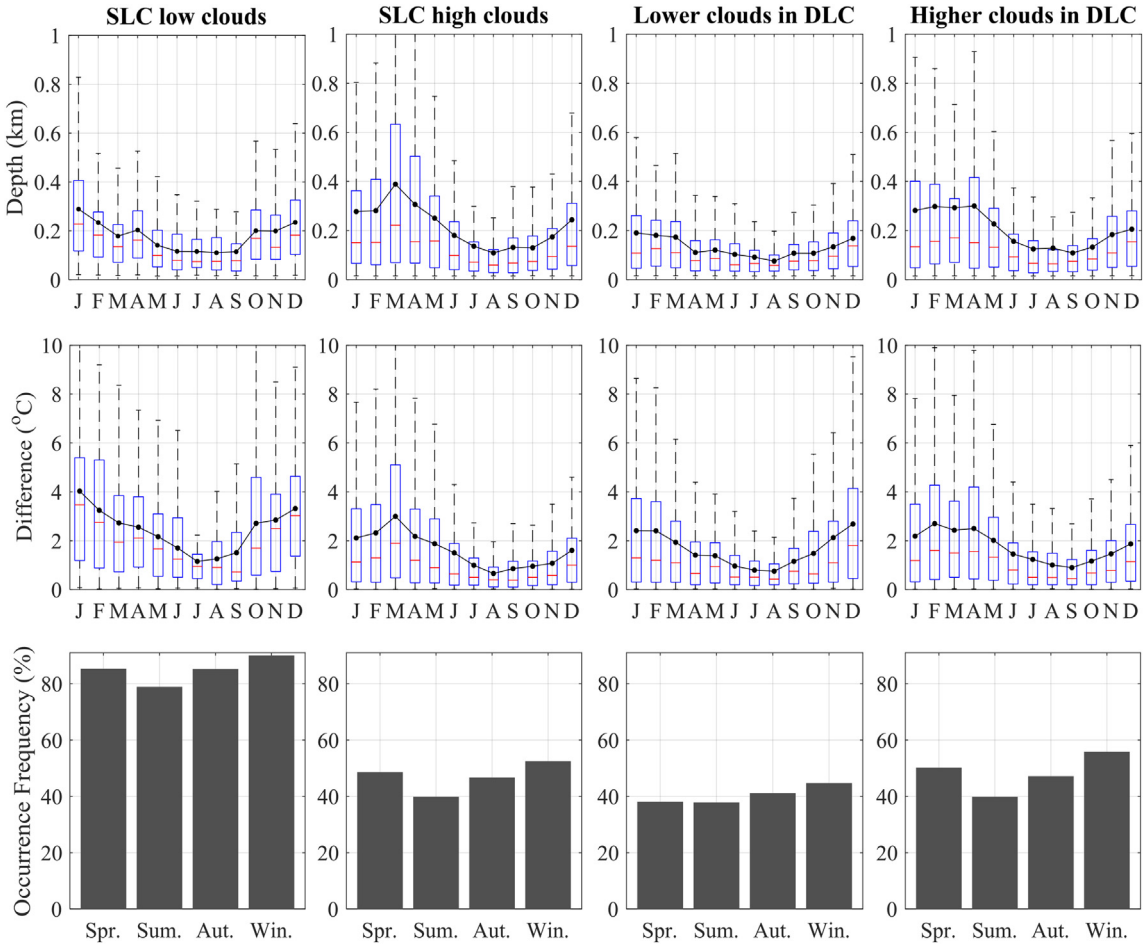

Fig. 6. Seasonal variations in temperature inversion properties in terms of depth (top panels), difference (middle panels), and occurrence frequency (bottom panels). Panels from left to right denote SLC low clouds, SLC high clouds, DLC lower clouds, and DLC higher clouds. The boxes in the top and middle panels indicate the 25th and 75th percentiles, the whiskers indicate the 5th and 95th percentiles, the horizontal lines inside the boxes indicate median values, and dots indicate mean values.

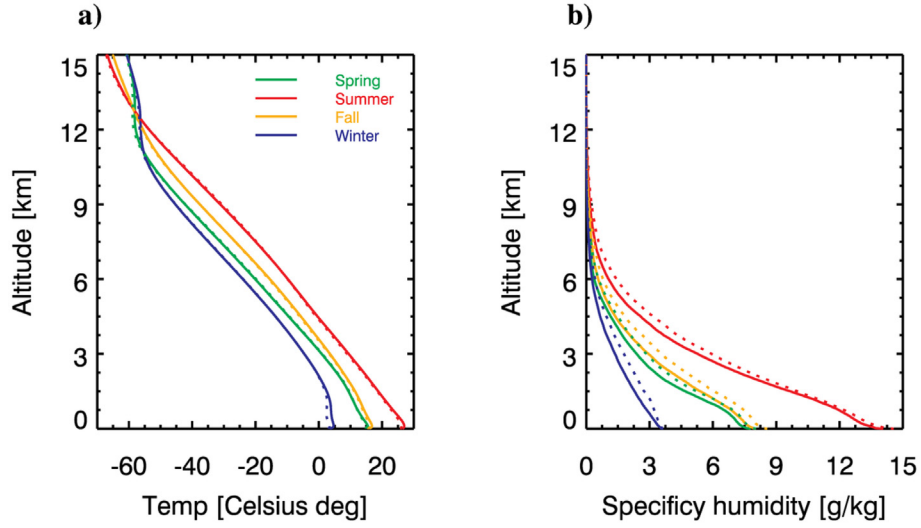

Fig. 7. (a) Temperature and (b) specific humidity profiles for SLC (solid curves) and DLC (dotted curves) from radiosonde measurements in spring (green), summer (red), autumn (orange), and winter (blue). (For interpretation of the references to colour in this figure legend, the reader is referred to the web version of this article.)

strengthen SW heating by allowing more incoming solar radiation to reach and be absorbed by clouds (Li and Moreau, 1996), the net effect is still negative (Table 2). If high clouds undergo stronger cloud-top radiative cooling, what causes the weaker and less frequent cloud-top temperature inversion? There are two possible reasons. First, high clouds undergo strong LW warming at their bases due to a larger temperature difference between the high cloud base and the warmer surface (Fig. 5a). This heating rate differentiation causes stronger in-cloud turbulent mixing that consumes the capping temperature inversion (Hartmann and Berry, 2017). Second, low SLC are mostly

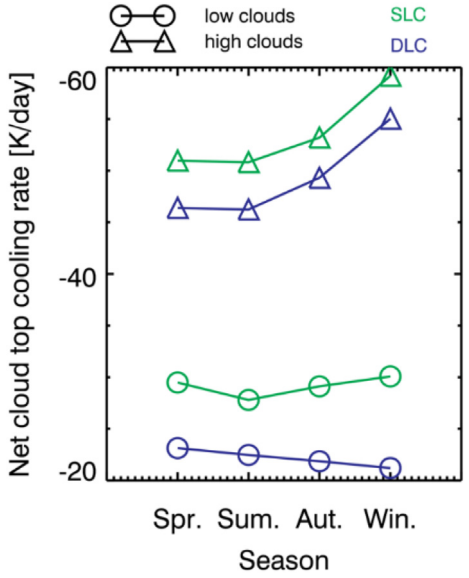

Fig. 8. Simulated seasonal cycles of net cloud-top radiative cooling for SLC (green) and DLC (blue). High (low) clouds are shown by curves with open triangles (circles). (For interpretation of the references to colour in this figure legend, the reader is referred to the web version of this article.)

boundary layer clouds and are often bounded by the ubiquitous temperature inversions that evolve from the radiative-cooling-induced surface layer inversion of the previous night (Stull, 1988). For SLC high clouds, the degree of cloud-top cooling should be weaker than the cooling of the surface because (1) the clouds are not always persistent so that the accumulation effect of LW cooling on the temperature inversion is undermined, and (2) the emissivity of clouds is generally smaller than that of the blackbody surface.

Fig. 5b shows that the LW cooling of SLC is considerably stronger than that of DLC lower clouds. The SW heating is also stronger in SLC, thus compensating to a certain degree the LW cooling. The net cooling of SLC is still stronger than the clouds in a DLC system (Table 2). This result is consistent with our theoretical analysis in Section 2 that an overlying cloud layer weakens the cooling of the underlying clouds and also the results from Christensen et al. (2013). To remove the potential radiative impacts of the moister atmosphere in DLC, we remove the overlying high cloud layer for the DLC case and obtain a radiative cooling profile very similar to that of SLC (Fig. 5b). This suggests that the presence of a high cloud layer is primarily responsible for the difference in radiative cooling. The moister free atmosphere plays a minor role.

3.4. Seasonal cycle

Fig. 6 presents the seasonal mean variabilities of temperature inversion parameters. These parameters vary in a similar manner. There is little variation until April when the magnitudes of the parameters start to decrease, reaching a minimum mid-year. Increases in the magnitudes of the parameters then follow. Overall, the three parameters show a strong seasonal variability with maxima in cold months (January, February, March, and December) and minima in warm months (June, July, August, and September).

What drives such distinctive seasonal cycles? To examine the degree to which cloud-top radiative cooling plays a role, we ran the SBDART radiative transfer model by ingesting the radiosonde-measured thermodynamic and moisture profiles (Fig. 7a and b) and cloud layers for each season and cloud regime. The calculated cloud-top radiative cooling can be considered as the maximum possible cooling under fully cloudy conditions. The solar zenith angles are specified as the noon times at the summer and winter solstices and the spring and autumnal equinoxes. The calculated SW fluxes, again, are divided by π to account for the diurnal cycle of the solar zenith angle. Radiative transfer simulations show that high clouds undergo considerably stronger cooling in winter than in summer (Fig. 8). Because the cloud-top temperature (or cloud emission) and above-cloud moisture loading (or downwelling radiation) have little seasonal variations, the contrast is primarily driven by SW heating because solar insolation is weaker in winter, allowing for more net radiative cooling. Spring and autumn lie somewhere in between but much closer to the summer values primarily because of the nonlinear dependence of the cloud-top radiative cooling on the solar zenith angle (Zhang et al., 2005; Zheng et al., 2016).

Compared with high clouds, the seasonal variation in cloud-top radiative cooling for low clouds is more difficult to assess because of the considerable seasonal cycles of all the influential parameters, i.e., cloud-top temperature [as seen from Fig. 7a, given that the low cloud-top heights (~2 km) do not change seasonally], above-cloud moisture loading (Fig. 7b), and solar insolation. The seasonal cycle of the low-cloud-top cooling is much weaker than that of both SLC and DLC high clouds (Fig. 8).

If the seasonal variation in cloud fraction was negligible, the calculated $CTRC^{*}_{NET}$ would not explain the strong seasonal variations in temperature inversions for all four cloud regimes (recall that the real spatially averaged cloud-top radiative cooling is the product of cloud fraction and $CTRC^{*}_{NET}$). This is particularly so for low clouds whose seasonal variation can have an amplitude as small as 10%. This motivates us to examine the cloud fraction seasonal cycle given that a larger cloud fraction enhances cloud-top cooling according to Eq. (2). Previous studies (e.g., Dong et al., 2005; Xi et al., 2010; Song et al., 2014; Kennedy et al., 2014) have shown that low- and high-cloud fractions have significant seasonal cycles, with cloud fractions being greater in winter than in summer by a factor of two or three. The cloud fraction impact on real spatially averaged cloud top radiative cooling outweighs the contribution from $CTRC^{*}_{NET}$. The seasonal pattern of cloud fraction [e.g., Fig. 1 in Song et al., 2014] matches well with the temperature inversions found in this study (Fig. 6). For a given region partially covered by clouds, a larger amount of clouds will make the overlying air cooler, enhancing the temperature inversion.

3.5. Diurnal cycle

Fig. 9 shows the diurnal variation in mean temperature inversion parameters and their standard deviations. Unlike the generally coherent seasonal cycles shown in Fig. 6, the diurnal cycles of different inversion parameters vary. It is well established, however, that clouds undergo considerable diurnal variations in radiative cooling with the weakest cooling at noon due to strong solar insolation (e.g., Zheng et al., 2016). Thicker dz above SLC tend to be reported in the early morning and at midnight relative to noon and afternoon (top panel of Fig. 9). For the DLC configuration, the diurnal variation in dz of the lower clouds varies less than that of the higher clouds. The dT of SLC low clouds is higher in magnitude than that of the three other cloud types.

How clouds adjust on a diurnal timescale may explain why the diurnal cycles of temperature inversion parameters are not as coherent as the seasonal cycles. Assuming that the degree of cooling of the air at the top of an inversion is negligible compared with the strong cooling of air adjacent to the cloud tops, we can relate the inversion intensity (ΔT) to cloud-top radiative cooling by the following relation:

$$d(\Delta T)/dt = CTRC_{NET} - B, \quad (3)$$

where B stands for the buffering effect arising from the adjustment of the system as a response to changes in $CTRC_{NET}$ and the resultant ΔT. This adjustment can include changes in cloud properties and the strength of turbulent mixing (i.e., the change in $CTRC_{NET}$ that modifies the instability of the cloud layer and thus the cloud-top entrainment warming).

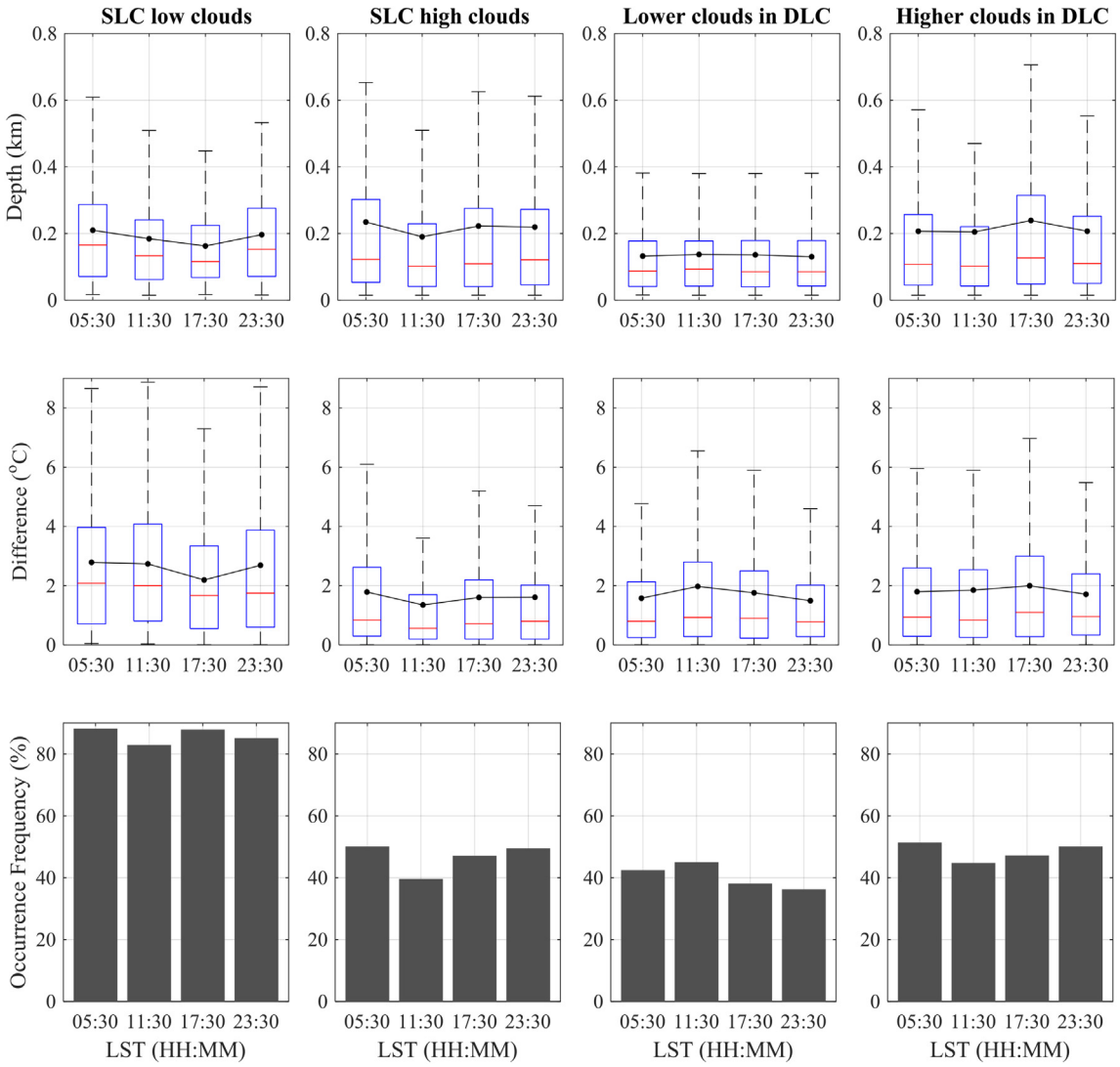

Fig. 9. Similar to Fig. 6 but for the diurnal cycle.

From a climatological point of view, the system is considered to be in equilibrium. So $CTRC_{NET}$ should be associated with ΔT in a climatological mean sense. On a diurnal timescale, however, the system is far from being in equilibrium. In a transient state, the characteristics of the buffering term, *B*, largely determine the relationship between ΔT and $CTRC_{NET}$. This term, however, is too complicated to be quantified by the observational analysis presented in this study. We are considering doing a follow-on modeling study using numerical models to further elucidate the diurnal behavior of inversion layers at cloud tops.

4. Conclusions and discussions

The characteristics of temperature inversions and radiative effects above clouds are closely related. On the one hand, temperature inversions over clouds can largely alter the radiative properties of the clouds. On the other hand, cloud-top radiative cooling plays a key role in the formation and maintenance of the temperature inversion. By analyzing 17 years (January 2001 to December 2017) of high-quality, long-term continuous radiosonde measurements collected at the ARM SGP site, this study characterizes temperature inversions above SLC and DLC and their temporal variability. Radiosonde measurements at a 10-m vertical resolution are used to retrieve cloud layer boundaries and locations of temperature inversions simultaneously. This removes potential biases caused by the mismatch of the two retrievals on spatial and temporal scales. Any variations in temperature inversion parameters according to cloud category are investigated.

For SLC, the occurrence frequency decreases dramatically from 85.5% to 46.5% as cloud tops rise from low to high altitudes. For DLC, a stronger temperature inversion is found for the higher cloud in terms of occurrence frequency, depth, and difference, due to the radiative energy interactions between the two layers of clouds. A distinctive seasonal cycle of cloud-top radiative cooling was revealed by the high clouds, primarily driven by SW heating variations. The seasonal variation for low clouds was associated with the seasonal variation in cloud fraction. How clouds adjust on a diurnal timescale can explain the mixed results regarding the diurnal cycle of temperature inversions.

The findings presented here are based on measurements from a single location in the mid-latitudes. Due to the limitation of point measurements, the results and conclusions from this study might only represent the local environmental effect on temperature inversion above cloud near the ARM SGP site. Future investigations will focus on different geographic locations with different climate regimes, such as the ARM Tropical Western Pacific site located in the core of the Pacific oceanic warm pool, and the high-altitude North Slope of Alaska site. This will further clarify the general representativeness of the findings under different climate regimes. Given the threshold limit of cloud thicknesses used by the radiosonde-based cloud retrieval method, it might miss very thin layer clouds. We will pair the radiosonde data with

lidar data at SGP site to help improve our understanding of these sub-visibile clouds in the future work. Moreover, potential evaporative cooling associated with the wet-bulb effect as the radiosondes emerge from cloud layers is not considered in this study given the extreme difficulty of quantifying it in observations. As the next step, it might be expected to quantitatively address this challenging issue through the combination of laboratory tests, in-situ experimental measurements and simulator/model simulations. Radiosonde data have been collected routinely for many decades by the World Meteorological Organization at widely dispersed upper-air sounding stations. Global descriptions of the thermal properties above clouds from these radiosonde measurements should be useful for validating global climate models, especially in their treatments of clouds and interactions with radiative processes.

Declaration of Competing Interest

The authors declare that they have no known competing financial interests or personal relationships that could have appeared to influence the work reported in this paper.

Acknowledgments

Data from the U.S. Department of Energy's Atmospheric Radiation Measurement (ARM) Climate Research Facility located near Lamont, Oklahoma were used in this study. This work was supported by the Strategic Priority Research Program of Chinese Academy of Sciences (Grant No. XDA17010101), the National Natural Science Foundation of China (Grant No. 41875183), and the National Key R&D Program of China (Grant No. 2017YFA0603504).

References

Bourne, S.M., Bhatt, U.S., Zhang, J., Thoman, R., 2010. Surface-based temperature inversions in Alaska from a climate perspective. Atmos. Res. 95 (2010), 353–366.
Bradley, R.S., Keiming, F.T., Diaz, H.F., 1992. Climatology of surface-based inversions in the North American Arctic. J. Geophys. Res.-Atmos. 97 (15) 699–15.
Bretherton, C.S., Wyant, M.C., 1997. Moisture transport, lower-tropospheric stability, and decoupling of cloud-topped boundary layers. J. Atmos. Sci. 54, 148–167.
Chernykh, I.V., Eskridge, R.E., 1996. Determination of cloud amount and level from radiosonde soundings. J. Appl. Meteorol. 35, 1362–1369.
Christensen, M.W., Carrió, G.G., Stephens, G.L., Cotton, W.R., 2013. Radiative impacts of free-tropospheric clouds on the properties of marine stratocumulus. J. Atmos. Sci. 70 (10), 3102–3118.
Del Genio, A.D., Wolf, A.B., Yao, M.S., 2005. Evaluation of regional cloud feedbacks using single-column models. J. Geophys. Res.-Atmos. 110 (D15).
Dong, X.Q., Minnis, P., Xi, B.K., 2005. A climatology of midlatitude continental clouds from the ARM SGP Central Facility: part I: Low-level cloud microphysical, microphysical, and radiative properties. J. Clim. 18 (9), 1391–1410.
Dong, X.Q., Xi, B.K., Minnis, P., 2006. A climatology of midlatitude continental clouds from the ARM SGP Central Facility. Part II: Cloud fraction and surface radiative forcing. J. Clim. 19, 1765–1783.
Fochesatto, G.J., 2015. Methodology for determining multilayered temperature inversions. Atmos. Meas. Tech. 8 (5), 2051–2060.
Ghate, V.P., Albrecht, B.A., Miller, M.A., Brewer, A., Fairall, C.W., 2014. Turbulence and radiation in stratocumulus-topped marine boundary layers: a case study from VOCALS-REx. J. Appl. Meteorol. Climatol. 53, 117–135.
Hartmann, D.L., Berry, S.E., 2017. The balanced radiative effect of tropical anvil clouds. J. Geophys. Res.-Atmos. 122, 5003–5020.
Jensen, M.P., Holdridge, D.J., Survo, P., Lehtinen, R., Baxter, S., Toto, T., Johnson, K.L., 2016. Comparison of Vaisala radiosondes RS41 and RS92 at the ARM Southern Great Plains site. Atmos. Meas. Tech. 9, 3115–3129.
Kalesse, H., Kollias, P., 2013. Climatology of high cloud dynamics using profiling ARM Doppler radar observations. J. Clim. 26, 6340–6359.
Kazil, J., Feingold, G., Yamaguchi, T., 2016. Wind speed response of marine non-precipitating stratocumulus clouds over a diurnal cycle in cloud-system resolving simulations. Atmos. Chem. Phys. 16 (9), 5811–5839.
Kennedy, A.D., Dong, X.Q., Xi, B.K., 2014. Cloud fraction at the ARM SGP site: instrument and sampling considerations from 14 years of ARSCL. Theor. Appl. Climatol. 115, 91–105.
Klein, S.A., Hartmann, D.L., 1993. The seasonal cycle of low stratiform clouds. J. Clim. 6, 1587–1606.
Li, Z., Moreau, L., 1996. Alteration of atmospheric solar absorption by clouds: simulation and observation. J. Appl. Meteorol. 35, 653–670.
Li, J., Chen, H., Li, Z., Wang, P., Cribb, M., Fan, X., 2015. Low-level temperature inversions and their effect on aerosol condensation nuclei concentrations under different large-scale synoptic circulations. Adv. Atmos. Sci. 32 (7), 898–908.
Lolli, S., Di Girolamo, P., Demoz, B., Li, X., Welton, E.J., 2017. Rain evaporation rate estimates from dual-wavelength lidar measurements and intercomparison against a model analytical solution. J. Atmos. Ocean. Technol. 34 (4), 829–839.
Mapes, B.E., Zuidema, P., 1996. Radiative-dynamical consequences of dry tongues in the tropical troposphere. J. Atmos. Sci. 53, 620–628.
Miller, N.B., Turner, D.D., Bennartz, R., Shupe, M.D., Kulie, M.S., Cadeddu, M.P., Walden, V.P., 2013. Surface-based inversions above Central Greenland. J. Geophys. Res.-Atmos. 118 (2), 495–506.
Minnis, P., Yi, Y., Huang, J., Ayers, J.K., 2005. Relationships between radiosonde and RUC-2 meteorological conditions and cloud occurrence determined from ARM data. J. Geophys. Res.-Atmos. 110 (D23).
Naud, C., Muller, J.P., Clothiaux, E.E., 2003. Comparison between active sensor and radiosonde cloud boundaries over the ARM Southern Great Plains site. J. Geophys. Res.-Atmos. 108 (D4).
Pithan, F., Medeiros, B., Mauritsen, T., 2013. Mixed-phase clouds cause climate model biases in Arctic wintertime temperature inversions. Clim. Dyn. 43, 289–303.
Ricchiazzi, P., Yang, S., Gautier, C., Sowle, D., 1998. SBDART: a research and teaching software tool for plane-parallel radiative transfer in the Earth's atmosphere. B. Am. Meteorol. Soc. 79 (10), 2101–2114.
Seidel, D.J., Ao, C.O., Li, K., 2010. Estimating climatological planetary boundary layer heights from radiosonde observations: comparison of methods and uncertainty analysis. J. Geophys. Res.-Atmos. 115, D16113.
Serreze, M.C., Kahl, J.D., Schnell, R.C., 1992. Low-level temperature inversions of the Eurasian Arctic and comparisons with Soviet drifting stations. J. Clim. 5, 615–630.
Solomon, A., Shupe, M.D., Persson, P.O.G., Morrison, H., 2011. Moisture and dynamical interactions maintaining decoupled Arctic mixed-phase stratocumulus in the presence of a humidity inversion. Atmos. Chem. Phys. 11, 10127–10148.
Song, H., et al., 2014. Evaluation of cloud fraction simulated by seven SCMs against the ARM observations at the SGP site. J. Clim. 27 (17), 6698–6719.
Stephens, G.L., Tsay, S., Stackhouse, P.W., Flatau, P.J., 1990. The relevance of the microphysical and radiative properties of cirrus clouds to climate and climatic feedback. J. Atmos. Sci. 47, 1742–1754.
Stephens, G.L., et al., 2012. An update on Earth's energy balance in light of the latest global observations. Nat. Geosci. 5, 691–696.
Stull, R., 1988. An Introduction to Boundary Layer Meteorology. Kluwer Academic Publishers, Dordrecht, The Netherlands.
Tobin, D.C., et al., 2006. Atmospheric Radiation Measurement site atmospheric state best estimates for atmospheric infrared sounder temperature and water vapor retrieval validation. J. Geophys. Res.-Atmos. 111 (D9).
Wang, J., Rossow, W.B., 1995. Determination of cloud vertical structure from upper air observations. J. Appl. Meteorol. 34, 2243–2258.
Wang, J., Rossow, W.B., Zhang, Y., 2000. Cloud vertical structure and its variations from a 20-year global rawinsonde dataset. J. Clim. 13, 3041–3056.
Wood, R., 2005. Drizzle in stratiform boundary layer clouds. Part I: Vertical and horizontal structure. J. Atmos. Sci. 62 (9), 3011–3033.
Wood, R., 2012. Stratocumulus clouds. Mon. Weather Rev. 140, 2373–2423.
Wood, R., Bretherton, C.S., 2006. On the relationship between stratiform low cloud cover and lower-tropospheric stability. J. Clim. 19, 6425–6432.
Wu, X., Park, S., Min, Q., 2008. Seasonal variation of cloud systems over ARM SGP. J. Atmos. Sci. 65 (7), 2107–2129.
Xi, B.K., Dong, X.Q., Minnis, P., Khaiyer, M.M., 2010. A 10-year climatology of cloud fraction and vertical distribution derived from both surface and GOES observations over the DOE ARM SPG site. J. Geophys. Res.-Atmos. 115 (D12).
Zhang, Y., Stevens, B., Ghil, M., 2005. On the diurnal cycle and susceptibility to aerosol concentration in a stratocumulus-topped mixed layer. Q. J. Roy. Meteor. Soc. 131 (608), 1567–1583.
Zhang, J., Chen, H., Li, Z., Fan, X., Peng, L., Yu, Y., Cribb, M., 2010. Analysis of cloud layer structure in Shouxian, China using RS92 radiosonde aided by 95 GHz cloud radar. J. Geophys. Res.-Atmos. 115 (D7).
Zhang, J., Li, Z., Chen, H., Cribb, M., 2013. Validation of a radiosonde-based cloud layer detection method against a ground-based remote sensing method at multiple ARM sites. J. Geophys. Res.-Atmos. 118 (2), 846–858.
Zhang, J., Li, Z., Chen, H., Yoo, H., Cribb, M., 2014. Cloud vertical distribution from radiosonde, remote sensing, and model simulations. Clim. Dyn. 43 (3–4), 1129–1140.
Zhang, J., Chen, H., Xia, X., Wang, W., 2016. Dynamic and thermodynamic features of low and middle clouds derived from Atmospheric Radiation Measurement Program mobile facility radiosonde data at Shouxian, China. Adv. Atmos. Sci. 33 (1), 21–33.
Zhang, L., Dong, X.Q., Kennedy, A., Xi, B.K., Li, Z., 2017. Evaluation of NASA GISS post-CMIP5 single column model simulated clouds and precipitation using ARM Southern Great Plains observations. Adv. Atmos. Sci. 34 (3), 306–320.
Zheng, Y., Rosenfeld, D., Li, Z., 2016. Quantifying cloud base updraft speeds of marine stratocumulus from cloud top radiative cooling. Geophys. Res. Lett. 43, 1567–1583.
Zheng, Y., Rosenfeld, D., Li, Z., 2018. The relationships between cloud-top radiative cooling rates, surface latent heat fluxes, and cloud-base heights in marine stratocumulus. J. Geophys. Res.-Atmos. 123, 11678–11690.
Zheng, Y., Rosenfeld, D., Zhu, Y., Li, Z., 2019. Satellite-based estimation of cloud top radiative cooling rate for marine stratocumulus. Geophys. Res. Lett. 46 (8), 4485–4494.